The Astrophysical Journal, 683:1168–1179, 2008 August 20

LARGE-SCALE CORONAL DENSITY AND ABUNDANCE STRUCTURES AND THEIR ASSOCIATION WITH MAGNETIC FIELD STRUCTURE

Yuan-Kuen Ko,[1,2] Jing Li,[3] Pete Riley,[4] and John C. Raymond[1]
Received 2007 November 27; accepted 2008 April 29

ABSTRACT

We construct subsynoptic maps of the ultraviolet-line fluxes, electron density, and elemental abundances for an east limb corona at 1.63 solar radii from 2000 September 20 to October 1. The data, covering position angles of 85°–126°, were taken from the Ultraviolet Coronagraph Spectrometer (UVCS) on board the *Solar and Heliospheric Observatory* (*SOHO*), and the maps are based on the variation of these parameters along the field of view of the UVCS slit. Combining these maps with the limb synoptic maps made from *SOHO* Extreme Ultraviolet Imaging Telescope, *SOHO* Large Angle and Spectrometric Coronagraph, and *Yohkoh* Soft X-ray Telescope observations provides a large-scale, distinct view of the contrast between different coronal structures in different physical properties and their relation to the underlying disk and magnetic field structures. During this time period, the east limb corona mainly consisted of three streamers and two dark areas that exhibited very different plasma properties. We construct a three-dimensional MHD coronal model that incorporates energy transport processes, and compare the large-scale coronal properties of the model with those of the observation. The comparison investigates areas of different abundances and densities, and their possible association with open and closed magnetic field structures. We find a good indication that the open field regions, which we believe to be the slow-wind source regions in this case, have lower coronal density and higher abundance values than the closed field regions. This is true for absolute abundance, and probably also for the FIP bias. Therefore, such synoptic maps can be very useful for identifying solar wind source regions.

Subject headings: solar wind — Sun: abundances — Sun: corona — Sun: UV radiation

Online material: color figures

1. INTRODUCTION

The outer atmosphere of the Sun exhibits various structures, such as active regions, coronal holes, filaments, quiet Sun, and streamers. Morphologically, these structures differ in appearance when observed by different means. This results from different physical properties (such as temperature, density, and abundance) in these structures, which are intimately associated with the underlying magnetic properties. For example, active regions generally contain high-temperature and dense plasma. They are usually observed to be bright in wavelengths that are emitted by ions of higher ionization (and therefore higher electron temperature; e.g., Feldman et al. 1998b, 1999; Ko et al. 2002), a characteristic believed to be related to the stronger magnetic field strengths in active regions (e.g., Golub et al. 1980; Yashiro & Shibata 2001). Active regions are also the regions of largest variability due to their having the most complicated and variable magnetic structure within. Coronal holes are, on the other hand, lower temperature, low-density regions and only show small-scale variability in both space and time. They are associated with open field lines and are the major source of the solar wind (e.g., Krieger et al. 1973). Quiet Sun is something in between in structural uniformity and variability. The magnetic structures within are small, low-lying loops that constitute the so-called magnetic carpet, which is found to evolve over a timescale of 40 hr (Title & Schrijver 1998). Filaments are low-temperature, high-density (compared to the surrounding corona) chromospheric material "floating" in the corona at an equilibrium state confined by the coronal magnetic field (Martin 1998). They are found to form along the neutral line of the solar magnetic field and are frequently associated with streamers and coronal mass ejections (CMEs) (e.g., Wright & McNamara 1983). Coronal streamers are distinct, high-density structures seen above the solar disk and beyond. The disk structures underlying the streamers are believed to be either active regions ("active region streamers") or structures that are associated with magnetic neutral lines ("quiescent streamers").

Elemental abundances also vary among the different coronal structures. The most frequently discussed abundance anomaly is the first ionization potential (FIP) effect (Meyer 1985), which measures the over/underabundance of the elements relative to their photospheric values. Elements with low FIP (<10 eV) are found to be overabundant by a factor (the so-called FIP bias) of 3–4 relative to those with high FIP (>10 eV) in active regions, quiet Sun, and streamers, and a factor of about 1 in coronal holes (see review in Raymond et al. 2001). On the other hand, the elemental composition of the solar wind also exhibits similar FIP bias, in that the low-FIP elements are enhanced relative to the high-FIP elements in the slow solar wind, while the FIP bias is smaller in the fast solar wind (Geiss et al. 1995; von Steiger et al. 2000). This results in a general belief in different coronal origins for these two distinct types of solar wind: that the fast solar wind originates within coronal holes and the slow solar wind is associated with open field regions near active regions, quiet Sun, and streamers. One other interesting finding is that, even though the FIP bias is similar in material of non–coronal hole origin, the absolute abundance (i.e., the abundance relative to hydrogen) is found to vary with heliocentric heights, and from structure to structure as well (Feldman et al. 1998a; Raymond 1999; Ko et al. 2002). In addition, Widing & Feldman (2001) found that the FIP bias, as dictated by the Mg/Ne ratios, changed for several newly emerging active regions from Mg/Ne ~1 to ~7–9 over the course of

[1] Harvard-Smithsonian Center for Astrophysics, 60 Garden Street, Cambridge, MA 02138.
[2] Current address: Space Science Division, Naval Research Laboratory, Washington, DC 20375.
[3] Institute for Astronomy, University of Hawaii, Honolulu, HI.
[4] Science Applications International Corporation, 10260 Campus Point Drive, San Diego, CA 92121.

3–7 days. Therefore, variations in elemental abundances can be useful for identifying various mechanisms that may govern the evolution of different coronal structures, as well as the solar wind.

In this paper, we construct subsynoptic maps of an east limb corona over the course of around 11 days. We use the observations by the Ultraviolet Coronagraph Spectrometer (UVCS) on board the *Solar and Heliospheric Observatory* (*SOHO*) to construct subsynoptic maps at 1.63 $R_\odot$ in the observed line intensities and the derived electron density and elemental abundances. Combining these maps with the limb synoptic maps made from *SOHO* Extreme Ultraviolet Imaging Telescope (EIT), *SOHO* Large Angle and Spectrometric Coronagraph (LASCO), and *Yohkoh* Soft X-ray Telescope (SXT) observations provides a large-scale, distinct view of the contrast between different coronal structures in different physical properties, and their relation to underlying disk and magnetic field structures. In § 2, we describe the data obtained from the *SOHO* UVCS. Section 3 presents the subsynoptic maps and discusses different physical properties among different coronal structures. In § 4, we construct a three-dimensional MHD model of the corona corresponding to this period and compare it to the observations. We also discuss the associated coronal magnetic field structures and implications related to the source of the solar wind. Section 5 gives some final remarks.

2. UVCS OBSERVATIONS

UVCS observations of this study were made from 2000 September 20 to October 1. The slit was situated at the heliocentric height of 1.63 $R_\odot$ at the east limb. The position angle (P.A.) was 110° (in the radial direction normal to the slit) for September 20, 18:36 UT–September 25, 18:03 UT, and 100° for September 25, 18:05 UT–October 1, 17:34 UT. The data reported here were taken from the O VI channel. The slit width was set to 100 μm, which corresponds to an instantaneous field of view (FOV) of 40′ by 28″. The data were obtained with a spatial binning of 3 pixels (21″). The grating position was set at 236,700, and the spectral lines observed were the O VI doublet $\lambda\lambda$1032, 1037, Lyβ, Lyγ, Si XII λ499, [Fe X] λ1028, Fe XV λ481, [Fe XVIII] λ974, and C III λ977. The spectral binning was 2 pixels, which corresponds to a resolution of 0.198 Å, except for Fe XV λ481, which was observed with a spectral binning of 3 pixels. For a detailed description of the UVCS instrument, see Kohl et al. (1995). The raw data were calibrated using the most recent UVCS data analysis software (DAS), version 4.0. The uncertainty in the flux calibration is about 20% for the first-order lines and 50% for the second-order lines (Gardner et al. 2000).

The 120 s exposures of the data were further combined into 126 1.45 hr–average (40 exposures) and 1.16 hr–average (32 exposures) files with 21″ spatial resolution to construct the fine-resolution line-flux maps, and 18 10 hr–average files with 63″ spatial resolution files to construct the density and abundance maps. Figure 1 shows the periods of data coverage for both time binnings.

The variations in time of the line flux for the O VI, Lyβ, and C III lines were inspected to identify transient brightenings from CMEs. Those exposures that show obvious transient signatures were deleted from the 10 hr–averaged data before combining the exposures.

We identified three transients on September 26 (19:53 UT–20:14 UT), September 30 (08:23 UT–09:13 UT), and September 30 (18:02 UT–18:09 UT), respectively. More often occurring are changes in the line flux caused by streamer deflection or blowout by the CMEs. These features are preserved in the presented data so as to show the morphology change in the constructed maps.

The mirror pointing was such that some amount of stray light was present in the data. Stray light correction was performed using

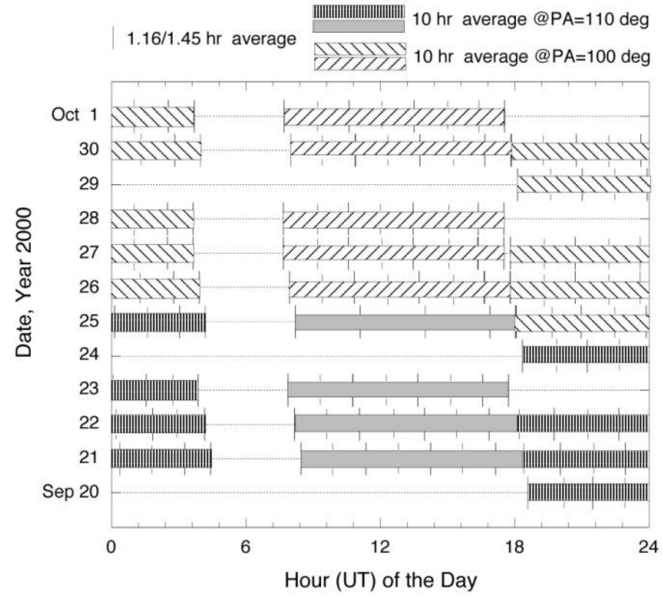

FIG. 1.—Periods of data covered for both pointings and time binnings. The shaded areas correspond to the 10 hr–averaged data. The 1.16/1.45 hr–averaged data periods are separated by vertical bars.

the C III λ977 line. The disk emission was calculated assuming the quiet Sun value (Vernazza & Reeves 1978) plus a contribution from an active region with an assumed radius of 0.1 $R_\odot$ (Ko et al. 2002). We find that the stray light contribution is <2% for the O VI lines and ~10% for Lyβ.

3. SUBSYNOPTIC CORONAL MAPS OF THE EAST LIMB FOR 2000 SEPTEMBER 20–OCTOBER 1

The UVCS observations presented here were made at two position angles (110° and 100°). Therefore, the FOVs of these two sets of data do not exactly overlap. In order to combine the two sets of data, we select a spatial region along the slit, such that the difference in the FOV is reasonably small. The regions selected for this study are P.A. = 86°–126° (spatial bin range 43–99) for the first set of data (September 20–25), and P.A. = 85°–125° (spatial bin range 30–86) for the second set of data (September 25–October 1). The difference in height between these two selected regions is less than 0.1 $R_\odot$, and the difference is more toward the two edges of the selected region. The line intensities and other physical quantities (electron density and abundance) along these selected spatial bins (or combined bins) are then stacked in subsequent order in time to construct the subsynoptic maps. These maps are very useful for illustrating the variation of the limb emission with time and P.A., and can be used to differentiate physical properties in different coronal structures.

3.1. *Line-Flux Maps*

The line flux in each spatial bin (21″) is obtained by summing over the counts across the line profile above a linear background level determined by the selected line-profile boundary. The line intensity in the combined spatial bin (63″) has better counting statistics and is obtained by a Gaussian fit with linear background. For strong lines such as the O VI doublets, Si XII, and Lyβ, the difference between the two fitting methods is mostly within 10%. Note that the measured line flux is the line emissivity integrated along the line of sight (see § 3.2).

Figure 2 shows the line-flux maps for O VI λ1032, Si XII λ499, Lyβ, [Fe XVIII] λ974, Fe XV λ481, and [Fe X] λ1028. The maps were constructed from the 1.45/1.16 hr–averaged data, with 21″

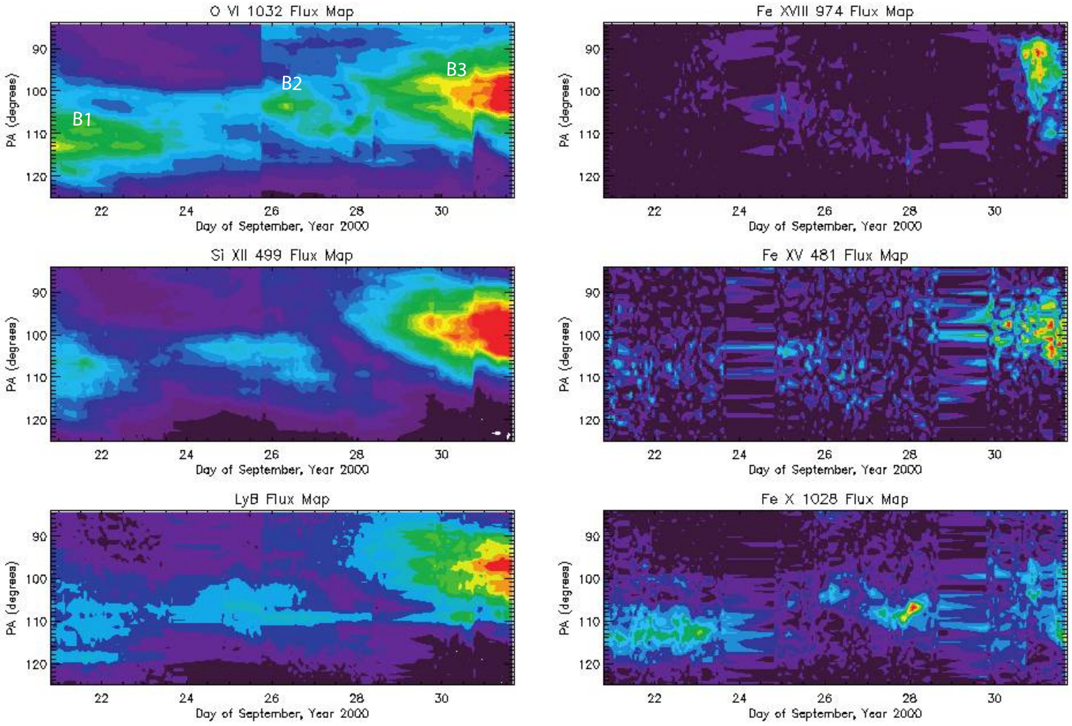

FIG. 2.—Line-flux maps for O VI λ1032, Si XII λ499, Lyβ, [Fe XVIII] λ974, Fe XV λ481, and [Fe X] λ1028. The maps are constructed from the 1.45/1.16 hr–averaged data, with 21″ spatial resolution. The discontinuity in intensity at 18:00 UT of September 25 is due to the change in the pointing (see text). There are two gaps in the data when the 24 hr synoptic observations were run (September 23, 17:44 UT–September 24, 18:21 UT, and September 28, 17:31 UT–September 29, 18:08 UT). The three bright structures, B1, B2, and B3 (see text), are marked on the O VI flux map. The spectrum of colors represents flux values from red (high) to purple (low).

spatial resolution. There is a discontinuity in intensity at 18:00 UT of September 25 that is due to the change in the pointing (mentioned above). There are two gaps in the data when the 24 hr synoptic observations were run (September 23, 17:44 UT–September 24 18:21 UT, and September 28, 17:31 UT–September 29, 18:08 UT), as can be seen more clearly in the Fe line-flux maps. The fluxes across the data gaps were interpolated from the data at the two ends of the gaps by the IDL routine that makes the image. Note that the intensities of these Fe lines are very weak, so the intensity values from these maps should not be considered accurate, except for those bins with the highest fluxes (shown in red/yellow). The purpose is to show the relative contrast in line emission, which is still a good indicator of which structure has stronger emission in these lines.

We can see that there are three main groups of bright structures (marked on the O VI line-flux map in Fig. 2). The first (structure "B1") appeared from the start of the observation until September 23 and was centered at P.A. $\sim 110^\circ$. The second (structure "B2") appeared after structure B1 from September 24 to 27 and was centered at around P.A. $= 105^\circ$. The third (structure "B3") appeared from September 29 until the end of the observation and was centered at around P.A. $= 100^\circ$. Structure B3 is particularly dense (or high in emission measure $\equiv \int n_e n_{\rm H}\, dl$) and hot according to the particularly bright emission exhibited by all the lines, including the high-temperature line [Fe XVIII] λ974. Structure B1 is probably the coolest of the three, judging from the brighter [Fe X] line emission there.

There are also several low-emission areas. The dark areas around September 23 at P.A. $\sim 90^\circ$ (north of structure B1) and around September 24–26 at P.A. $\sim 120^\circ$ (south of structure B2) probably relate to a midlatitude coronal hole and its extension at the equatorial region. Note, however, that these dark areas seen at the limb would correspond to mixed emissions along the line of sight from the coronal hole and the surrounding brighter structures. There is another dark area around September 30–October 1 at P.A. $\sim 120^\circ$ (south of structure B3). We find that these dark areas are associated with low electron density, and that some are associated with high elemental abundances (see §§ 3.2 and 3.3).

Figure 3 shows the limb synoptic maps (LSMs; Li et al. 2000) constructed from the EIT 195, 284, 171, and 304 Å, *Yohkoh* SXT/AlMg, and LASCO C2 images. These LSMs were constructed by summing over the signals within an arc of a given width (i.e., height) and length (i.e., P.A.) range for each time-sequence image, and stacking them with time. The selected height range for the EIT LSMs is 1.35–1.365 $R_\odot$, that for the *Yohkoh* SXT LSM is 1.0–1.015 $R_\odot$, and that for the C2 LSMs is 2.50–2.55 $R_\odot$. The selected P.A. range is 65°–155°. The white box indicates the time and P.A. covered by the UVCS maps (Fig. 2). These LSMs also show three bright coronal structures and dark areas that closely correspond to the UVCS maps. This correspondence is especially clear for the EIT LSMs. The strong emission in EIT 284 Å in structure B3 relative to the other two structures agrees with the interpretation of the UVCS maps that the electron temperature there is particularly high. One exception is in the EIT 171 Å map, where the brightest emission lies where all other emission is faint (September 30–October 2, P.A. $\sim 120^\circ$). This indicates that the coronal temperature distribution along the line of sight in that region has a particularly cool (around or below 1 MK) component and is depleted at the higher temperature range seen in other EIT wave bands (1.5–2 MK). The particularly bright white-light emission in structure B3 shown in the C2 map indicates that the emission measure (and probably the electron density itself) is much higher than in the corona at other times and locations, which is also consistent with the UVCS maps. The morphology shown in the C2 map is less similar to that of the UVCS and EIT maps. The bright structures seen by C2 are what we usually call "streamers,"

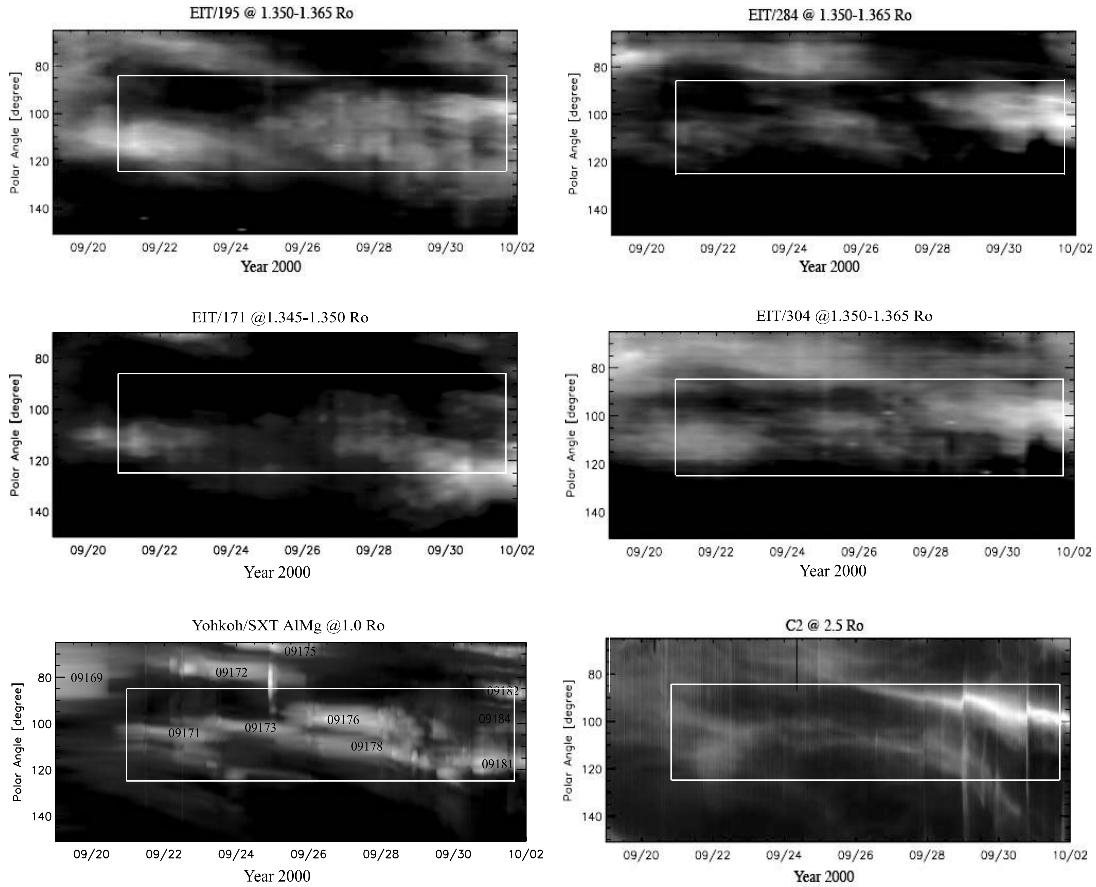

Fig. 3.—Limb synoptic maps constructed from EIT 195, 284, 171, and 304 Å, *Yohkoh* SXT/AlMg, and LASCO C2 images. The white box indicates the time and spatial coverage of the UVCS data. [*See the electronic edition of the Journal for a color version of this figure.*]

which in general are narrower (in latitude) than their corresponding structures at lower heights. On the other hand, maps at lower heights show more complex morphology within the wider structure, due to multiple loop structures that can be resolved by those instruments.

The SXT LSM images are marked with the active region number. SXT images are good for identifying the location of active regions, because these structures often emit strong soft X-rays due to the existence of high-temperature plasma. We can see that structure B2 is directly above the active regions 9173, 9176, and 9178. Structure B1, on the other hand, is not directly above any active regions, but rather is above some non–spot magnetic concentration/filament area, which may explain its cooler temperature. Structure B3 lies right between active regions (ARs) 9181 and 9182, and is possibly associated with AR9184. It is worthwhile to note that the sudden brightening of AR9182 in the SXT LSM is from the postflare loops of a flare/CME on September 30 from this AR, and that the region with strong EIT 171 Å emission mentioned above (September 30–October 2, P.A. $\sim 120°$) lies just to the south of this region.

One interesting feature is the displacement of the streamer or loops by the CME. The white vertical stripes in the C2 maps indicate CMEs. We can see that the east limb corona was fairly quiet until after September 28, when several very bright CMEs passed through that part of the corona. We can see clear deflection of the streamers on the C2 map. For example, the streamer (which corresponds to structure B3) was substantially deflected by two CMEs early on September 29 and late on September 30, but was not disrupted. The deflection of the loop structure at lower height can also be clearly seen in both the EIT and UVCS maps for the September 30 CME. One other interesting feature is a very strong emission of the [Fe x] line that appeared at P.A. $\sim 110°$ for about 12 hr from late September 27 until the middle of September 28, and that moved northwards by about 5° during that time. The same feature can also be seen in the O vi map, but it does not stand out in the Lyβ map. We have seen several cases of cool, localized emission appearing after a CME (e.g., Ciaravella et al. 2002; Ko et al. 2003). However, there was no major eruption during that time except a small puffing around the streamer at P.A. $= 110°$ in LASCO C2. EIT images do not show obvious eruptions either.

There was a very localized prominence at about the same P.A. late on September 27, as can be more clearly seen in He i λ10830 from the Mauna Loa Solar Observatory (MLSO). This cool [Fe x] feature disappeared around 08:00 UT on September 28 when a small CME (possibly associated with that prominence) occurred there at about the same time.

3.2. *Electron Density Map*

For most lines observed by the UVCS, emission is produced by electron collisional excitation followed by spontaneous emission. The emission-line flux under the isothermal approximation is

$$I_{\rm coll} = \frac{1}{4\pi}\frac{A_{\rm el}}{A_{\rm el,\,phot}} h\nu_{\rm line}\varepsilon(T_e) n_e n_{\rm H} L \ \ {\rm erg\ cm^{-2}\ s^{-1}\ sr^{-1}}, \quad (1)$$

where $A_{\rm el} \equiv n_{\rm el}/n_{\rm H}$ is the elemental abundance relative to hydrogen (i.e., absolute abundance) and $A_{\rm el,\,phot}$ is its photospheric value.

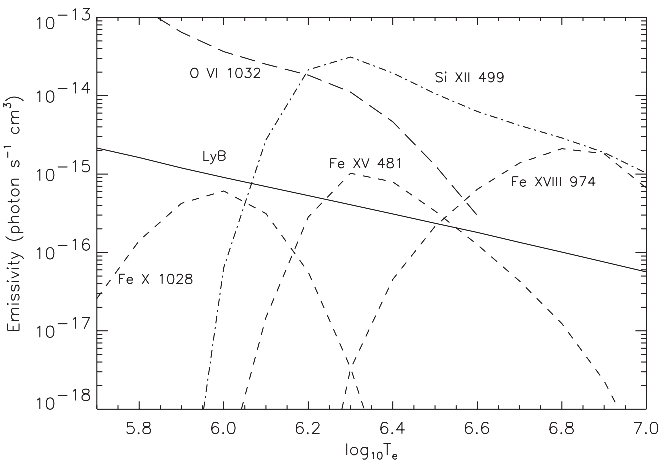

FIG. 4.—Emissivities for lines observed in this data set.

The parameter $\varepsilon(T_e)$ is the emissivity (or contribution function), which is defined as

$$\varepsilon(T_e) = A_{\mathrm{el,phot}}\, y_{\mathrm{ion}}(T_e) B_{\mathrm{line}}\, q_{\mathrm{line}}(T_e), \quad (2)$$

where $y_{\mathrm{ion}}(T_e) \equiv n_{\mathrm{ion}}/n_{\mathrm{el}}$ is the ionic fraction, which is a function of the electron temperature T_e, B_{line} is the branching ratio for the line transition, and $q_{\mathrm{line}}(T_e)$ is the electron excitation rate, which is a function of only the electron temperature T_e in the low-density limit. Figure 4 plots ε as a function of T_e for the lines observed in this data set. The quantity $n_e n_{\mathrm{H}} L$ is the emission measure (in cm^{-5}) at the given electron temperature, and L is the effective line-of-sight distance. The emissivities are calculated from the CHIANTI database, version 5.01 (Dere et al. 1997; Landi et al. 2006), and we use the ionization equilibria from Mazzotta et al. (1998). The photospheric abundances are adopted from Grevesse & Sauval (1998) except for that of oxygen, which is adopted from Asplund et al. (2004).

For certain lines such as the hydrogen Lyman series and the O VI $\lambda\lambda$1032, 1037 doublet, the emission produced by radiative scattering of the chromospheric emission can contribute significantly to the total coronal emission. It can be written as (Noci et al. 1987)

$$I_{\mathrm{rad}} = \frac{1}{4\sqrt{\pi}} \frac{\lambda_{\mathrm{line}}}{\nu_{\mathrm{line}}} \frac{\pi e^2}{m_e c} f_{\mathrm{line}} B_{\mathrm{line}} (A_{\mathrm{el}}\, y_{\mathrm{ion}} n_{\mathrm{H}} L) h(r) \times \frac{I_{\mathrm{disk}}}{\sqrt{\left(\Delta\lambda_{\mathrm{cor}}^2 + \Delta\lambda_{\mathrm{ex}}^2\right)}} D(v_{\mathrm{out}}) \ \mathrm{erg\ cm^{-2}\ s^{-1}\ sr^{-1}}, \quad (3)$$

where f_{line} is the oscillator strength (0.0791 for Lyβ; 0.131 for O VI λ1032), B_{line} is the branching ratio (0.88 for Lyβ; 1 for O VI λ1032), and I_{disk} (in erg s^{-1} cm^{-2} sr^{-1}) is the disk intensity, which is calculated by assuming quiet Sun plus an AR of size 0.1 $R_\odot$ (see Ko et al. 2002 for model details). We then have $I_{\mathrm{disk}} = 359$ erg s^{-1} cm^{-2} sr^{-1} for O VI λ1032 and $I_{\mathrm{disk}} = 885$ erg s^{-1} cm^{-2} sr^{-1} for Lyβ, which can be compared to the quiet Sun values of 305 and 747 erg s^{-1} cm^{-2} sr^{-1}, respectively (Vernazza & Reeves 1978). The term $\Delta\lambda_{\mathrm{ex}}$ is the e^{-1} half-width of the disk line, which is 0.121 Å for O VI λ1032 (Doschek & Feldman 2004) and 0.18 Å for Lyβ (assuming a thermal width of 1.6×10^5 K). The term $\Delta\lambda_{\mathrm{cor}}$ is the e^{-1} half-width of the coronal absorption profile, which we adopt from the measured line profiles (0.183 Å for O VI λ1032 and 0.431 Å for Lyβ). The quantity $\pi(R_\odot/r)^2 h(r) \equiv 2\pi\{1 - [1 - (R_\odot/r)^2]^{1/2}\}$ is the solid angle subtended by the solar disk at a distance r, which is 1.63 $R_\odot$ in this case, and $D(v_{\mathrm{out}})$ is the Doppler dimming factor (Strachan et al. 1993), which depends on the radial outflow speed v_{out}, as well as on the disk emission and coronal absorption profiles. Under the condition of zero outflow, $D(v_{\mathrm{out}}) = 1$.

The electron density can thus be estimated by taking the ratio of equation (1) over equation (3). We use the O VI λ1032 line to calculate the electron density this way. The radiative and collisional components of O VI λ1032 can be separated using the O VI $\lambda\lambda$1032, 1037 doublet, given that the doublet ratio of O VI λ1032/λ1037 from the radiative component is 4, and that from the collisional component is 2 (e.g., Raymond et al. 1997). Even though we have three Fe lines, their emissivity peaks are too far apart to obtain confident estimates for T_e (see Fig. 4). Furthermore, the counting statistics of the Fe XV and [Fe XVIII] lines are poor for most space-time bins of the map (see Fig. 2). Past UVCS observations in streamers around 1.6 $R_\odot$ yield a log T_e in the 6.0–6.3 range, i.e., 1×10^6–2×10^6 K (e.g., Ko et al. 2002; Bemporad et al. 2003; Uzzo et al. 2004). We thus assume log $T_e = 6.15$ (1.4×10^6 K; see also discussions in § 3.3). When there is no better estimate of T_e at each bin of the map, assuming a constant T_e, though probably far from realistic, has the advantage that it makes it easier to see the deviation from what is presented here in case other values of T_e should be adopted. Nevertheless, the resulting n_e is not sensitive to the electron temperature, since y_{ion}, which contributes to the strongest T_e dependence in both I_{coll} and I_{rad} for O VI λ1032 in the MK gas, cancels out while taking the ratio. On the other hand, the resulting n_e strongly depends on the assumed I_{disk} and $D(v_{\mathrm{out}})$.

Figure 5 plots the resulting electron density map at 1.63 $R_\odot$. It is constructed from the 10 hr–averaged data with 63″ spatial resolution. We assume $D(v_{\mathrm{out}}) = 1$ here. The maximum and minimum values for n_e are 9.15×10^6 and 1.03×10^6 cm^{-3}, respectively. We can see that the three bright structures have high electron densities, while the mentioned dark areas have low electron densities. There is an interesting low-density "dark lane" feature in the northwest-southeast direction from September 26 to October 1 between structures B2 and B3. The bright Fe X emission "spot" mentioned above seems to have lower n_e, which would require even lower T_e in order to produce the observed Fe X emission.

It is worth noting that any density measurement by remote sensing is a weighted average along the line of sight. The UVCS density is an average weighted by the O VI intensity, which drops off around r^{-4} at these heights, while the C2 density is an average weighted by the dilution factor for disk radiation, which drops off more slowly than r^{-2}. Therefore, the UVCS density is much more strongly weighted toward the lowest height along the line of sight, which is the plane of the sky. This also helps to explain why the C2 structure (Fig. 3) lasts longer than the corresponding UVCS structure (e.g., 4 days seen by C2 vs. 2 days seen by the UVCS for structure B3).

Also plotted in Figure 5 is the O VI λ1032/λ1037 ratio. The maximum and minimum values are 3.4 and 2.4, respectively. This implies that the outflow velocity is less than 100 km s^{-1} for all coronal structures at this height, since for $V_{\mathrm{out}} > 100$ km s^{-1}, the pumping of O VI 1037.61 Å by C II 1037.02 Å would drop the doublet ratio to below 2 (Noci et al. 1987). Note that the O VI doublet ratios show anticorrelation with the electron density, in that a higher n_e corresponds to a lower O VI doublet ratio. This is because a higher n_e implies a larger contribution from the collisional component (see eqs. [1] and [3]). The radial outflow speed would have similar anticorrelation, in that higher outflow reduces the contribution from the radiative component. Therefore, $D(v_{\mathrm{out}})$, and thus the doublet ratio, decreases with increasing V_{out} (valid for $V_{\mathrm{out}} < 100$ km s^{-1}).

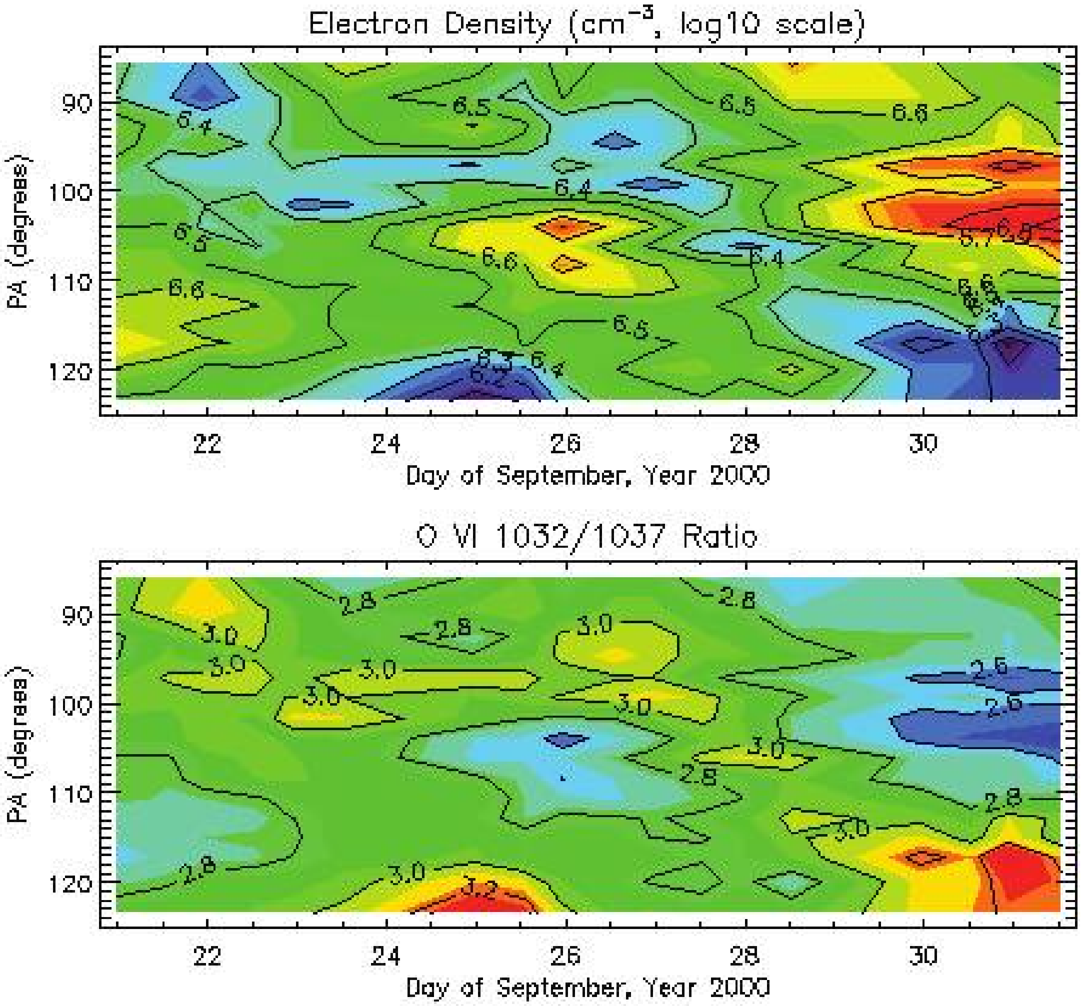

FIG. 5.—Electron density and O VI $\lambda1032/\lambda1037$ ratio maps at 1.63 $R_\odot$. The figure is constructed from the 10 hr–averaged data, with 63″ spatial resolution. Here, we assume $D(v_{\rm out}) = 1$ and $\log T_e = 6.15$ across the whole map (see discussions in § 3.2). The spectrum of colors represents values from red (high) to purple (low). The corresponding numerical values are marked on the contour curves. The maximum and minimum values for n_e are 9.15×10^6 and 1.03×10^6 cm^{-3}, respectively. The maximum and minimum values for the O VI $\lambda1032/\lambda1037$ ratios are 3.4 and 2.4, respectively.

Figure 5 assumes that $D(v_{\rm out}) = 1$ and that the O VI doublet ratios constrain the outflow speed to be less than 100 km s^{-1}. For a quiescent corona at 1.63 $R_\odot$, the outflow speed is expected to be well below 100 km s^{-1}, even in coronal holes (e.g., Cranmer et al. 1999; Miralles et al. 2001). Previous analyses of coronal streamers usually took $D(v_{\rm out}) = 1$ as a good approximation. Here, we discuss the effect of the existence of outflows on the derived n_e. For an outflow speed of 50 km s^{-1}, $D(v_{\rm out})$ is about 0.75, as modeled by Dodero et al. (1998) for values of $\Delta\lambda_{\rm ex}$, $\Delta\lambda_{\rm cor}$, and height similar to those in this data set. This would imply an n_e lower than that shown in Figure 5 by the same factor. We would expect outflows to exist in open field regions in coronal holes, or adjacent to the boundary of a streamer or AR. If we suppose that the dark (also lower n_e) regions in Figure 2 are possible locations for open field regions, then outflows there would decrease the resulting n_e, thus further enhancing the density contrast exhibited in Figure 5.

3.3. *Elemental Abundance Maps*

The elemental abundances relative to H (absolute abundance) and O (the FIP bias) can be calculated from the line ratios to Lyβ and O VI $\lambda1032$ using equation (1), again under the isothermal assumption. The collisional and radiative components of Lyβ are separated using equations (1) and (3) with the derived n_e (assuming no Doppler dimming). Note that if $D(v_{\rm out}) < 1$ at certain regions (see discussions in § 3.2), the collisional component of Lyβ would decrease by about a similar factor, thus increasing the resulting O/H by a factor of about $1/D(v_{\rm out})$. Since the Lyβ coronal absorption profile is wider than that of O VI, the effect of outflow is significantly smaller for Lyβ. Figure 6 plots the line-flux map for O VI $\lambda1032$ and O/H at 1.63 $R_\odot$, using the 10 hr–averaged, 63″ spatial resolution data. Note that the change in $\varepsilon_{{\rm Ly}\beta}/\varepsilon_{\rm O\,VI\,\lambda1032}$ from 1×10^6 to 2×10^6 K (relative to that for 1.4×10^6 K) is less than 30% (see Fig. 4). Therefore, the O/H abundance is not sensitive to the assumed T_e values, even under the condition that the T_e distribution is not isothermal.

It can be seen that the O/H abundance is very nonuniform among these coronal structures. The location of high/low emission of the O VI line can be compared with that of high/low O/H. We note that the regions of the highest O/H abundance are those of low O VI emission and low electron density (see Figs. 5 and 6). The three bright streamer structures exhibit different O/H values. For instance, structure B3 is depleted in O/H; one possible cause for this is the gravitational settling in closed loop structures (e.g., Raymond et al. 1997; Ko et al. 2002; Uzzo et al. 2004). On the other hand, O/H in structure B1 is higher than that in B3 by about a factor of 2. Structure B2 is more complex and exhibits low abundance and high density first (September 24–26), then high

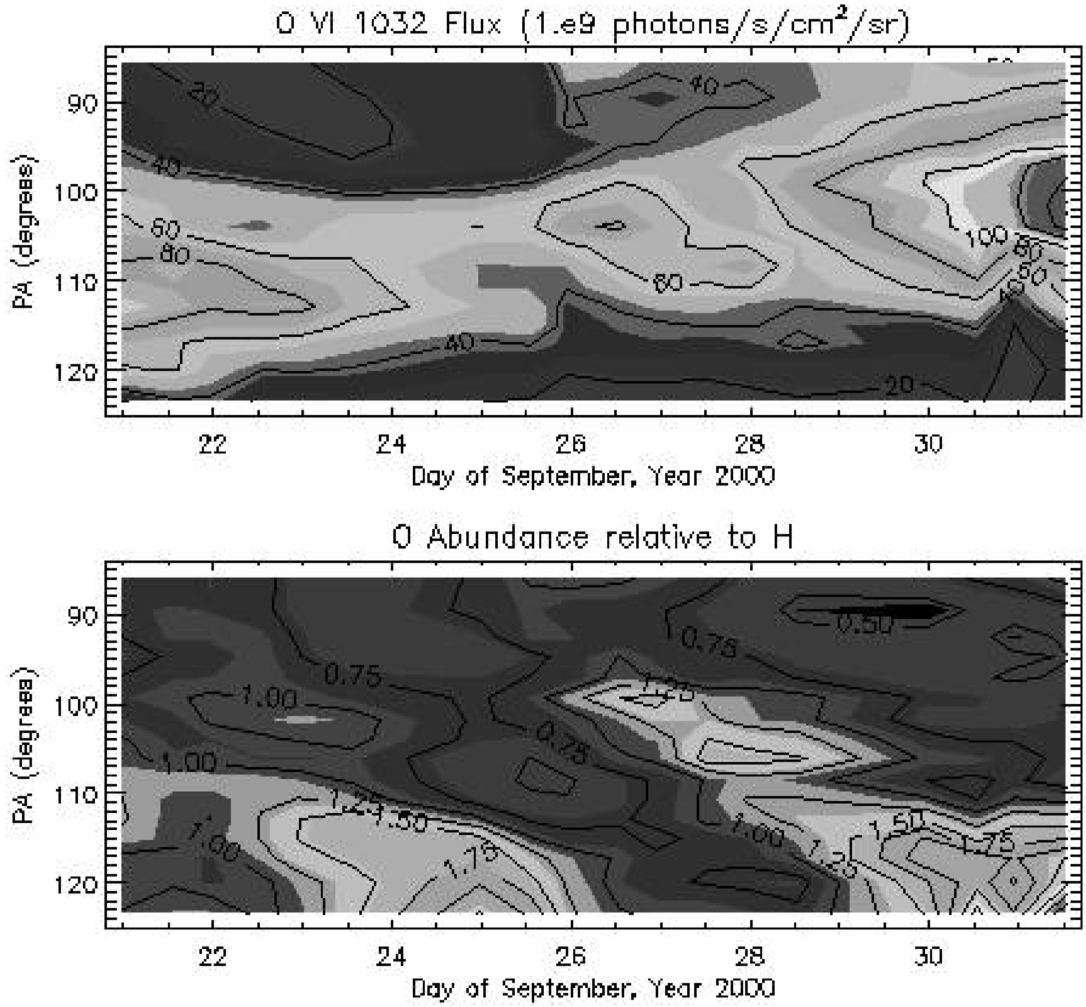

FIG. 6.—Line-flux map for O VI λ1032 and O/H (at 1.63 $R_\odot$) using the 10 hr–averaged data, with 63″ spatial resolution. The spectrum of colors represents values from red (high) to purple (low). The corresponding numerical values are marked on the contour curves. The maximum and minimum values for O/H are 3.24 and 0.41, respectively. [*See the electronic edition of the Journal for a color version of this figure.*]

abundance and low density later (September 26–28). Since the abundance difference across the map is more than a factor of 3, and the counting statistics for both lines are very good, we are confident that the abundance structure shown in Figure 6 is real and not affected by uncertainty in the line measurements or the assumed T_e.

The same method can be applied to produce the X/H and X/O abundance maps of Si and Fe. However, the results are very sensitive to the assumed T_e, because the emissivities of Si XII λ499 and [Fe X] λ1028 in the usual coronal temperature range (1×10^6–2×10^6 K) are very sensitive to T_e (see Fig. 4), especially for Si XII. For illustration purposes, Figure 7 shows the Si and Fe abundance maps relative to H and O, assuming $T_e = 1.4 \times 10^6$ K. We can see that the Fe/H (and most Si/H) structure is similar to O/H in that the abundance is among the lowest in structure B3, and the lowest density areas have the highest abundance. Fe/O and Si/O, however, show nearly opposite structure in general; i.e., high- (low-) Fe/O areas exhibit low (high) Si/O. Since both Fe and Si are low-FIP elements, this unexpected result is probably due to variations in T_e.

There are still some constraints that can be considered.

1. The isothermal assumption is probably not realistic, whether along the line of sight, or among structures. If the emission-measure distribution were flat in the 1×10^6–2×10^6 K range, the Fe X line would mainly be produced in the $\sim 10^6$ K plasma, while the Si XII line would mainly be produced in the $\sim 2 \times 10^6$ K plasma. It may be especially true in those areas where X/O > 10, which is rarely reported in past observations. Those areas probably have some higher T_e gas, where most Si XII emission is produced and where the Si abundances would be lower than those shown here (and vice versa for Fe/O).

2. The T_e in areas with significant [Fe XVIII] emission (e.g., structure B3; see Fig. 2) is probably higher than assumed, which is not the case for those areas with low [Fe XVIII] emission. In this case, for example, we expect that the Si/H and Si/O abundances in structure B3 can be a lot lower than what is shown in Figure 7. Since the emissivities for the [Fe X] and Si XII lines change in a direction opposite to that of T_e (in the 1×10^6–2×10^6 K range; see Fig. 4), it can somewhat constrain the allowed T_e range of the multi-T_e distribution, since the resulting abundance could otherwise be unrealistically high. In all, more accurate information about the T_e distribution along the line of sight is needed to obtain more accurate abundances for Si and Fe for this data set.

In another approach, we first derive the T_e at which Fe/O $=$ Si/O, based on the justification that the FIP effect should be similar for Fe and Si because both are low-FIP elements. The resulting maps for T_e, Fe/O (which is presumed to be equal to Si/O), O/H, and Fe/H are shown in Figure 8. Note that n_e and the

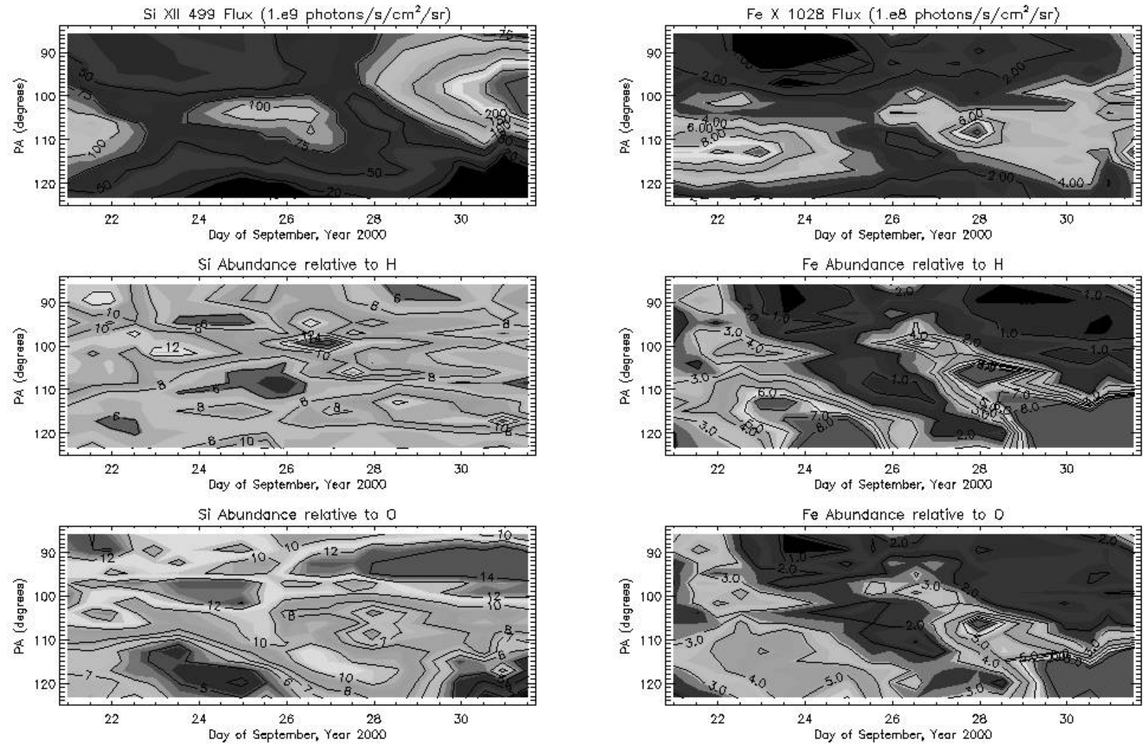

FIG. 7.—Line-flux maps of Si XII λ499 and [Fe X] λ1028, and the abundance maps for Si and Fe relative to H and O using the 10 hr–averaged data, with 63″ spatial resolution. The parameter T_e is assumed to be 1.4×10^6 K everywhere. The spectrum of colors represents values from red (high) to purple (low). The corresponding numerical values are marked on the contour curves. The maximum values for Si/H, Si/O, Fe/H, and Fe/O are 17.7, 17.3, 27.1, and 11.6, respectively. The minimum values for Si/H, Si/O, Fe/H, and Fe/O are 4.26, 2.10, 0.48, and 0.86, respectively. [*See the electronic edition of the Journal for a color version of this figure.*]

collisional component of Lyβ all need to be recalculated in this case. Also note that since we use the [Fe X] and Si XII lines here, the resulting T_e would only represent those plasmas at around the maximum formation temperature of the two lines, which is around 1–2 MK (see Fig. 4). The resulting n_e and O/H are changed by less than 4%, which is expected, since they are insensitive to T_e in the range of concern. We can see that T_e is higher for structures B2 and B3, which is consistent with the fact that the [Fe XVIII] emission is also brighter there, although, as noted above, the T_e obtained here probably does not reflect the actual high-temperature plasma corresponding to the [Fe XVIII] emission. The value of T_e is lowest where n_e and the line intensities are also at their lowest values. This is consistent with the view that those areas are probably associated with some coronal hole material along the line of sight. Fe/H shows structure similar to O/H. The structure of both Fe/H and Fe/O is similar to that shown in Figure 7, with an assumption of constant T_e, except that the range of values is smaller. This demonstrates that the sensitivity of the T_e-dependence of these line emissivities is a major source of uncertainty in determining the abundances from these specific Fe and Si lines. We believe that Fe and Si abundances obtained using this method are more reliable than those obtained using a constant-T_e assumption.

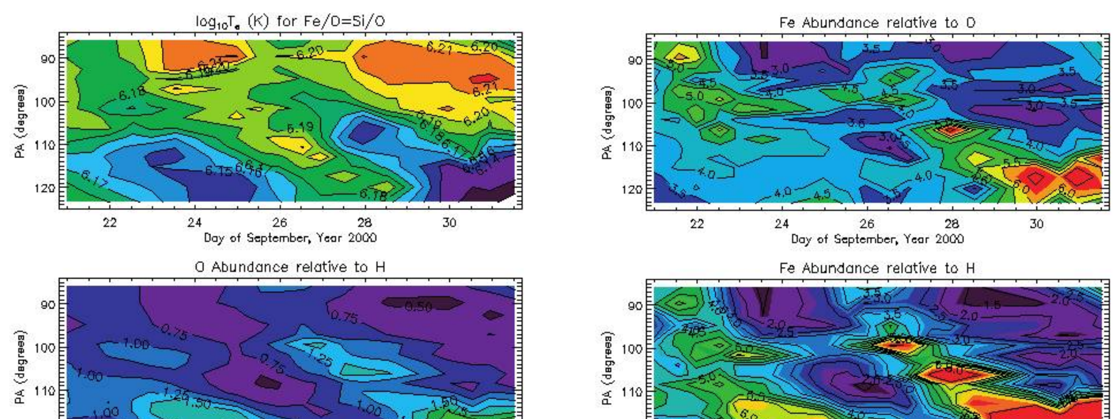

FIG. 8.—*Top left*: Electron temperatures at which Fe/O = Si/O. *Top right*: Fe/O (=Si/O) in this case (see § 3.3). *Bottom*: Resulting O/H and Fe/H at these electron temperatures. The spectrum of colors represent values from red (high) to purple (low). The corresponding numerical values are marked on the contour curves. The maximum values for T_e, O/H, Fe/H, and Fe/O are 1.68×10^6 K, 3.25, 17.3, and 8.74, respectively. The minimum values for T_e, O/H, Fe/H, and Fe/O are 1.31×10^6 K, 0.42, 1.27, and 2.40, respectively.

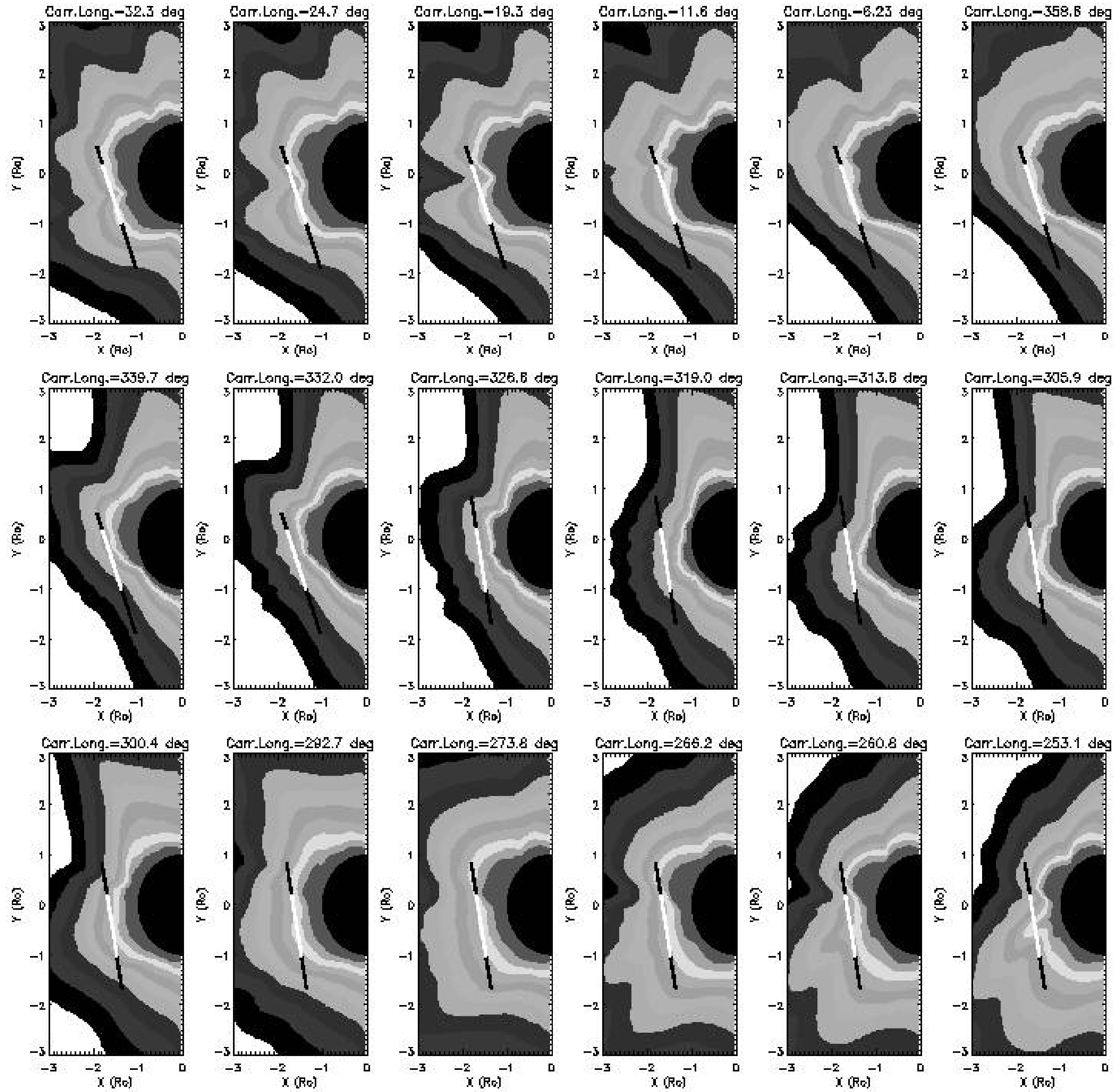

FIG. 9.—Electron density contours at 18 Carrington longitudes corresponding to the 18 UVCS data periods. The UVCS slit position is overlaid on each of the contour images. The white area is the portion of the slit extracted for analysis. The Carrington longitude marked on each panel is that of the east limb structure observed at the disk center around 7 days later. The observations started at Carrington rotation 1967, at a longitude of 32.3°, and ended at Carrington rotation 1968, at a longitude of 253.1°. [*See the electronic edition of the Journal for a color version of this figure.*]

That the FIP bias (as seen from Fe/O) is highest in the low-n_e region is interesting. One possibility is that this region is the source of the slow solar wind from the boundaries between coronal holes and ARs (Ko et al. 2006), where the FIP effect is expected, and where the electron temperature in the open field region is simply lower than that in the adjacent closed loops. This is opposite to what is observed in low-density regions deep within polar or equatorial coronal holes, from which we would expect fast solar wind and the FIP bias to be small here (e.g., von Steiger et al. 2000). One other possibility is that the two dark areas have broad emission-measure distributions, such that the [Fe X] and Si XII lines come from different parts of the T_e distribution. This would invalidate the underlying assumption of this approach that both lines are produced from the same material along the line of sight. For example, there may be more low-T_e material that emits [Fe X] than high-T_e material that emits Si XII along the line of sight of these dark areas. In that case, Fe/O values would be smaller than those obtained in Figure 8.

4. COMPARISON WITH A 3D MHD MODEL

We have shown in previous sections how different coronal structures are related to different physical properties. Now we

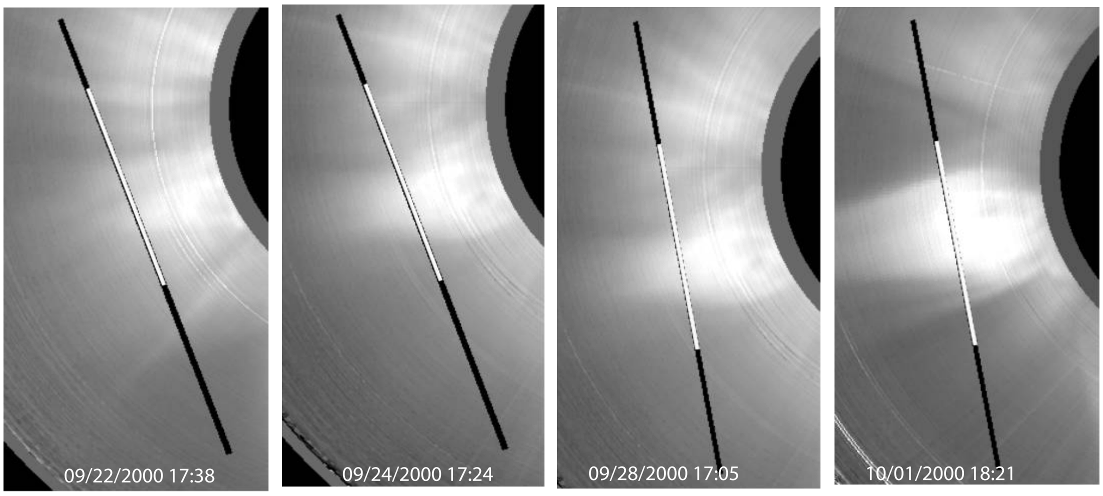

Fig. 10.—MLSO MK4 white-light images of the east limb corona for 2000 September 22, 24, 28, and October 1. The UVCS slit position is plotted on the images, and the white area is the portion of the slit extracted for analysis (cf. Fig. 9). These images can be compared with the electron density contours from the model in Fig. 9, specifically, those with Carrington longitudes of 11.6° (CR 1967; MK4 image of September 22), 339.7° (CR 1968; MK4 image of September 24), 292.7° (CR 1968; MK4 image of September 28), and 253.1° (CR 1968; MK4 image of October 1).

want to ask whether they are related to the underlying magnetic structures, and if so, how they are related. To investigate these questions, we construct a 3D MHD model of the corona for that time period.

The 3D MHD coronal model used in this study is similar to that described by Lionello et al. (2001). It differs from earlier, polytropic versions of the model (e.g., Mikić & Linker 1996; Linker et al. 1999) in that it incorporates energy transport processes, including thermal conduction, radiation, and coronal heating. An Alfvén wave pressure is also included to provide acceleration of the wind. In addition, the base of the calculation is set in the upper chromosphere, allowing us to model the transition region, albeit in an idealized way. For this study, a nonuniform grid 125 points in radius, 99 points in latitude, and 125 points in longitude is used. Because the observations span two Carrington rotations (CRs 1967 and 1968), we construct a specific Carrington map spanning from the 140° Carrington longitude of CR 1967 to the 140° Carrington longitude of CR 1968. Note that the Carrington longitudes correspond to those of east limb structures observed at the disk center around 7 days later (i.e., offset by about −90° in longitude, as counted from the observing dates).

In order to compare the electron density structures of the model with those of the data, we interpolate the model values among the model grid positions that correspond to positions along the UVCS slit. Figure 9 shows the electron density contours from the model. Each panel corresponds to the east limb plane of the sky at each of the 18 UVCS observation time periods (see Fig. 1). These contours are overlaid with the corresponding UVCS slit positions, as seen in the plane of the sky. The white portion of the slit is the spatial extent presented in this paper (i.e., P.A. $= 85°-126°$). To help visualize the east limb corona during this period, Figure 10 shows the MLSO MK4 white-light images for 2000 September 22, 24, 28, and October 1. The UVCS slit position is plotted on the images and, as in Figure 9, the white area is the portion of the slit extracted for analysis. These images can be compared to the electron density structure of the east limb plane of the sky obtained from the model (Fig. 9), specifically, to that with Carrington longitudes of 11.6° (CR 1967; MK4 image of September 22), 339.7° (CR 1968; MK4 image of September 24), 292.7° (CR 1968; MK4 image of September 28), and 253.1° (CR 1968; MK4 image of October 1). Figure 10 can also be compared with the subsynoptic maps (Figs. 2, 3, and 5). We can see that the MK4 images are consistent with these observations, but that not all are similar to the model results, which we will discuss in more detail below.

Figure 11 shows the electron density contours versus time and P.A. from the 3D MHD model constructed from Figure 9. This figure is to be compared with the observations shown in Figure 5. What we look for is the large-scale difference among structures at various times and locations. Comparing the values of the density is not the purpose of this study. In fact, we cannot expect the data and the model to match closely in magnitude. To achieve this would require fine tuning the input parameters in the model, such as those for the heating function, which would require a great deal of computation time. Furthermore, such comparison is inherently limited by the 7 day difference between the observations and the input magnetogram, a time during which the solar structures may change significantly. We see that the large-scale structure of the coronal density does not, in general, match well between the data and the model, which is not surprising given the limitations discussed above. However, there are similarities, such as higher density near the locations of structures B1 and B3, and relatively low density regions at September 22 (P.A. $\sim 90°$), September 25 (P.A. $\sim 120°$), and October 1 (P.A. $\sim 120°$).

Figure 12 shows the input magnetic field B_r from the disk magnetogram at 1 $R_\odot$ (*top*), and the field-line structure (open vs. closed) at the model grid of 1.624 $R_\odot$ (closest to the UVCS observing

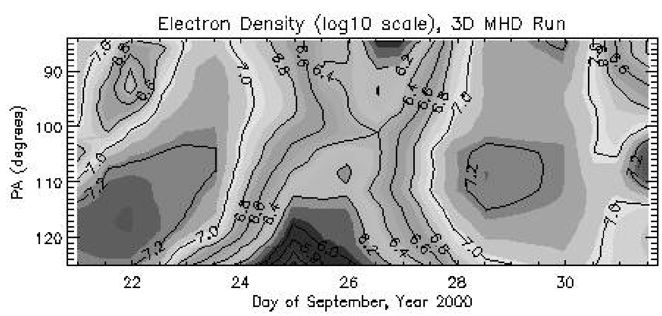

Fig. 11.—Electron density contours vs. P.A. and date constructed from the 3D MHD model shown in Fig. 9. Compare these with the density contours from UVCS observations (Fig. 5). [*See the electronic edition of the Journal for a color version of this figure.*]

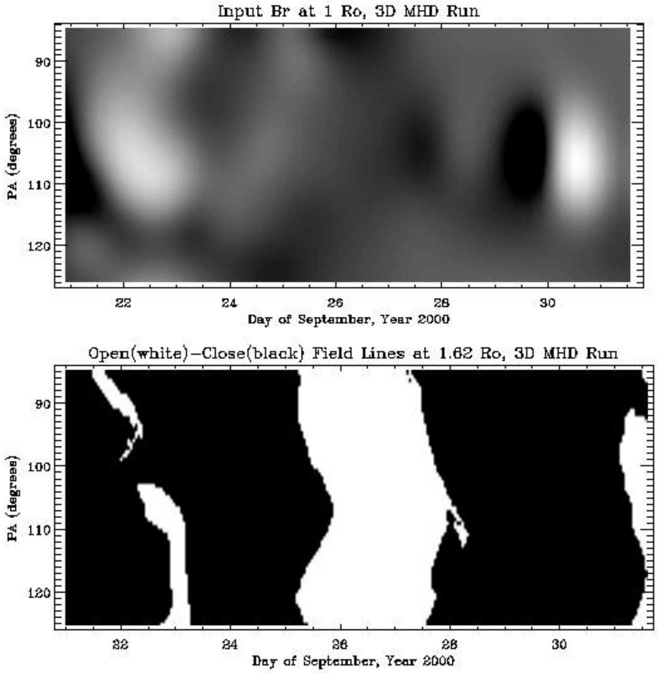

FIG. 12.— *Top*: Input magnetic field B_r from the disk magnetogram at 1 $R_\odot$, from the 3D MHD model. *Bottom*: Field-line structure (open vs. closed) at 1.624 $R_\odot$, from the 3D MHD model.

height) (*bottom*). The electron density structure from the model basically reflects the magnetic field structure, with the open field regions having lower density than the closed field regions. Although it is not possible at this time to make a clear one-to-one comparison between the coronal structures from the data and the field-line structures from the model, there is a good indication that the bright, high-density structures seen by the UVCS are indeed closed field regions, and that those dark regions with low density and high abundance are associated with open field regions. Further examination of disk images indicates that those low-density, high-abundance regions are likely associated with some low-latitude coronal holes. We believe that these regions are the boundaries between the coronal hole and the AR loops, and are probably a source of the slow solar wind. Even if these coronal holes are also fast wind sources, the emission associated with the fast wind is probably much lower and masked by the brighter emission at the boundary (Ko et al. 2006).

5. FINAL REMARKS

It is commonly understood that there are various types of structures in the solar corona, and that the physical properties of these structures, namely temperature, density, and abundance, can vary by a wide range, even within similar types. This set of data shows us just that. In addition, these data allow us to look into the variations in a large, continuous span in space and time, as opposed to snapshots of individual structures at different times. We have also attempted to find characteristics in these coronal properties that may be directly associated with the magnetic field structure. Our analyses indicate that open field regions, i.e., the slow wind source regions in this case, are of lower coronal density and have higher abundance values than closed field regions. This is true for absolute abundance and probably the FIP bias also. Therefore, the synoptic maps presented here can be very useful for identifying solar wind source regions.

One may argue that some variations exhibited in these maps come from the line-of-sight effect. It is certainly true that some continuous changes seen across two distinct structures, especially along the time axis, are due to changes in the line of sight with time, which contains different fractions of the two structures at each instant. However, it is also hard to imagine that, in reality, each structure has only one density value, abundance value, etc., with abrupt changes between structures, and that the line-of-sight effect is the sole cause for the intermediate values between the structures. In our opinion, it is more likely that the physical properties across the boundaries between structures, e.g., across open and closed field regions, should change in a somewhat gradual way. It remains to be investigated how great the spatial extent of such a boundary can be.

Such synoptic maps in physical parameters provided from spectroscopic data are valuable empirical constraints for improving coronal models. For example, the density and temperature structures can be used to refine the heating function in the 3D MHD model presented in this study. The variation in the corona reflects the variation in the solar wind. Material that becomes the solar wind can be released from a variety of solar structures that have been shown to exhibit a wide variety of physical properties whose values are derived by spectroscopic means (e.g., electron density, ion and electron temperatures, and elemental abundances). Therefore, spectroscopic diagnostics of these structures, combined with solar wind models and the in situ measurements of the solar wind, are very valuable for investigating the sources of the solar wind. This study is geared toward this effort. It is hoped that when more consistent results are achieved between coronal field models and observations, we can make more confident and direct comparisons with the solar wind data, and we will be a step closer to understanding how the solar wind is formed.

Y.-K. K. would like to thank J. Linker for valuable discussions. This project is supported by NASA grant NNX07AL72G. *SOHO* is a joint mission of the European Space Agency and NASA. Although not presented in this paper, we acknowledge the use of the MAS model results provided by the Community Coordinated Modeling Center (CCMC) at the Goddard Space Flight Center through their public Runs-on-Request system (http://ccmc.gsfc.nasa.gov/). The CCMC is a multiagency partnership between NASA, AFMC, AFOSR, AFRL, AFWA, NOAA, NSF, and ONR. The MAS Model was developed by J. Linker, Z. Mikić, R. Lionello, and P. Riley at the Science Applications International Corporation (SAIC), San Diego, California.

REFERENCES

Asplund, M., Grevesse, N., Sauval, A. J., Allende Prieto, C., & Kiselman, D. 2004, A&A, 417, 751

Bemporad, A., Poletto, G., Suess, S. T., Ko, Y.-K., Parenti, S., Riley, P., Romoli, M., & Zurbuchen, T. Z. 2003, ApJ, 593, 1146

Ciaravella, A., Raymond, J. C., Li, J., Reiser, P., Gardner, L. D., Ko, Y.-K., & Fineschi, S. 2002, ApJ, 575, 1116

Cranmer, S. R., et al. 1999, ApJ, 511, 481

Dere, K. P., Landi, E., Mason, H. E., Monsignori-Fossi, B. F., & Young, P. R. 1997, A&AS, 125, 149

Dodero, M. A., Antonucci, E., Giordano, S., & Martin, R. 1998, Sol. Phys., 183, 77

Doschek, G. A., & Feldman, U. 2004, ApJ, 600, 1061

Feldman, U., Curdt, W., Doschek, G. A., Schühle, U., Wilhelm, K., & Lemaire, P. 1998a, ApJ, 503, 467

Feldman, U., Doschek, G. A., Schühle, U., & Wilhelm, K. 1999, ApJ, 518, 500

Feldman, U., Schühle, U., Widing, K. G., & Laming, J. M. 1998b, ApJ, 505, 999

Gardner, L. D., Atkins, N., Fineschi, S., Smith, P. L., Kohl, J. L., Maccari, L., & Romoli, M. 2000, Proc. SPIE, 4139, 362

Geiss, J., Gloeckler, G., & von Steiger, R. 1995, Space Sci. Rev., 72, 49
Golub, L., Maxson, C., Rosner, R., Vaiana, G. S., & Serio, S. 1980, ApJ, 238, 343
Grevesse, N., & Sauval, A. J. 1998, Space Sci. Rev., 85, 161
Ko, Y.-K., Raymond, J. C., Li, J., Ciaravella, A., Michels, J., Fineschi, S., & Wu, R. 2002, ApJ, 578, 979
Ko, Y.-K., Raymond, J. C., Lin, J., Lawrence, G., Li, J., & Fludra, A. 2003, ApJ, 594, 1068
Ko, Y.-K., Raymond, J. C., Zurbuchen, T. H., Riley, P., Raines, J. M., & Strachan, L. 2006, ApJ, 646, 1275
Kohl, J. L., et al. 1995, Sol. Phys., 162, 313
Krieger, A. S., Timothy, A. F., & Roelof, E. C. 1973, Sol. Phys., 29, 505
Landi, E., Del Zanna, G., Young, P. R., Dere, K. P., Mason, H. E., & Landini, M. 2006, ApJS, 162, 261
Li, J., Jewitt, D., & LaBonte, B. 2000, ApJ, 539, L67
Linker, J. A., et al. 1999, J. Geophys. Res., 104, 9809
Lionello, R., Linker, J. A., & Mikić, Z. 2001, ApJ, 546, 542
Martin, S. F. 1998, Sol. Phys., 182, 107
Mazzotta, P., Mazzitelli, G., Colafrancesco, S., & Vittorio, N. 1998, A&AS, 133, 403
Meyer, J.-P. 1985, ApJS, 57, 173
Mikić, Z., & Linker, J. A. 1996, in AIP Conf. Proc. 382, Solar Wind Eight, ed. D. Winterhalter et al. (Woodbury: AIP), 104
Miralles, M. P., Cranmer, S. R., Panasyuk, A. V., Romoli, M., & Kohl, J. L. 2001, ApJ, 549, L257
Noci, G., Kohl, J. L., & Withbroe, G. L. 1987, ApJ, 315, 706
Raymond, J. C. 1999, Space Sci. Rev., 87, 55
Raymond, J. C., et al. 1997, Sol. Phys., 175, 645
———. 2001, in AIP Conf. Proc. 598, Solar and Galactic Composition, ed. R. F. Wimmer-Schweingruber (Melville: AIP), 49
Strachan, L., Kohl, J. L., Weiser, H., Withbroe, G. L., & Munro, R. H. 1993, ApJ, 412, 410
Title, A. M., & Schrijver, C. J. 1998, in ASP Conf. Ser. 154, Stellar Systems and the Sun, ed. R. A. Donahue & J. A. Bookbinder (San Francisco: ASP), 345
Uzzo, M., Ko, Y.-K., & Raymond, J. C. 2004, ApJ, 603, 760
Vernazza, J. E., & Reeves, E. M. 1978, ApJS, 37, 485
von Steiger, R., et al. 2000, J. Geophys. Res., 105, 27217
Widing, K. G., & Feldman, U. 2001, ApJ, 555, 426
Wright, C. S., & McNamara, L. F. 1983, Sol. Phys., 87, 401
Yashiro, S., & Shibata, K. 2001, ApJ, 550, L113